Effects of Transition-Metal V-Doping on the Structural, Magnetic and Transport Properties in La0.67Sr0.33MnO3 Manganite Oxide

4 AUTHORS:

S. Mnefgui
University of Monastir
13 PUBLICATIONS   61 CITATIONS

SEE PROFILE

A. Dhahri
monastir
39 PUBLICATIONS   262 CITATIONS

SEE PROFILE

Dhahri Jemai
University of Monastir
90 PUBLICATIONS   634 CITATIONS

SEE PROFILE

E.K. Hlil
French National Centre for Scientific Resea…
446 PUBLICATIONS   1,707 CITATIONS

SEE PROFILE

Effects of Transition-Metal V-Doping on the Structural, Magnetic and Transport Properties in La$_{0.67}$Sr$_{0.33}$MnO$_3$ Manganite Oxide

Safa Mnefgui · Abdessalem Dhahri · Jemai Dhahri · El-Kebir Hlil

Abstract We have investigated the structural, magnetic, and electrical transport properties of a series of ABO$_3$-type perovskite compounds, La$_{0.67}$Sr$_{0.33}$Mn$_{1-x}$V$_x$O$_3$ ($0 \leq x \leq 0.15$). The samples were characterized by X-ray diffraction and data were analyzed using Rietveld refinement technique, it has been concluded that these materials have the rhombohedral structure with R$\overline{3}$C space group. The magnetization and resistivity measurements versus temperature proved that all our samples exhibit a ferromagnetic to paramagnetic transition and a metallic to semiconductor one when the temperature increases. Both the Curie temperature T_C and the resistivity transition temperature T_P of the composites decrease, while the resistance increases as the V content increases. It has been concluded that the electrical conduction mechanism in the metallic regime at low temperatures ($T < T_P$) can be explained on the basis of grain boundary effects and the single electron-magnon scattering process. Resistivity data were well fitted with the relation $\rho = \rho_0 + \rho_2 T^2 + \rho_{4.5} T^{4.5}$, whereas the adiabatic Small Polaron Hopping (SPH) and Variable Range Hopping (VRH) models are found to fit well in the paramagnetic semiconducting regime at the high temperature ($T > T_P$).

Keywords Manganite · Vanadium · Rietveld refinement · Conduction mechanism · Variable range hopping

S. Mnefgui (✉) · A. Dhahri · J. Dhahri
Laboratoire de Physique des Solides, Département de Physique, Faculté des Sciences de Monastir, 5019 Monastir, Tunisia
e-mail: mnefguisafa@yahoo.fr

E.-K. Hlil
Institut Néel, CNRS-Université J. Fourier, B.P. 166, 38042 Grenoble, France

1 Introduction:

For nearly the last decade, there has been extensive research on ABO$_3$-type manganites of the general formula R$_{1-x}$A$_x$MnO$_3$ (R = La, Nd, Pr, Y, etc. and A = Ca, Sr, Ba, Pb, etc.). These compounds have attracted much attention due to their extraordinary magnetic and electronic properties as well as their promise for the potential technological applications [1–3]. The manganite system offers a high degree of chemical flexibility. This leads, together with a complex interplay between structures, electronic and magnetic properties, to a very rich phase diagram involving various metallic, insulating and magnetic phases [4]. These properties are sensitive to the doping concentration x, which determine the Mn^{3+}/Mn^{4+} ratio to maintain charge neutrality, the average cationic radii $\langle r_A \rangle$ and the ionic size mismatch between the various A-site ions, and it is represented by the variance $\sigma^2 = \sum_i y_i r_i^2 - \langle r_A \rangle^2$, where r_i corresponds to the radii of the various A-sites cations and y_i to their fractional occupancies ($\sum_i y_i = 1$) [5, 6]. When the antiferromagnetic insulator, LaMnO$_3$, is doped with the divalent ions (A^{2+}), it can be driven into a metallic ferromagnetic state due to conversion of proportional number of Mn^{3+} to Mn^{4+} through the so-called "double exchange (DE)" of the Mn^{3+}–O^{2-}–Mn^{4+} mechanism by Zener [7]. Because of the strong Hund's coupling, the electronic configurations are Mn^{3+} ($t_{2g}^3 e_g^1$) and Mn^{4+} ($t_{2g}^3 e_g^0$). The mobile e_g electrons produced due to the hole doping via DE mediate ferromagnetism and conduction. Previously, only these theories have used to explain the transport and magnetic properties of the manganites by suggesting that the mixed valence of Mn^{3+}/Mn^{4+} is a key component for understanding the ferromagnetic–paramagnetic (FM–PM) phase transition associated with an insulator–metal (IM) transition in these manganites and the CMR effect [8, 9]. But recent detailed research has shown

that these concepts are not sufficient to explain the details of the observed resistivity behavior, such as the insulating behavior above T_C, the mechanism of conduction, and the CMR. Some authors have proposed numerous other physical model and mechanisms, like the small polaron, the electron-electron scattering, the magnon correlated transport [10–12] and the phase separation [13–15] models in order to give a more complete explanation of a variety of phenomena observed in manganites.

Among these perovskite-type manganites, $La_{1-x}Sr_x$ MnO_3 with $x \approx 1/3$ has the highest Curie temperature ($T_C \sim 365$ K) and remarkable CMR effect [16, 17] which make it a potential material candidate for technological applications. Structural, magnetic and transport properties of $La_{1-x}Sr_xMnO_3$ with $x \approx 1/3$ can be considerably affected by the substitution of Mn with various other metallic elements such as Fe [18, 19], Ni [20, 21], Ti [22], Al [23, 24] and Cu [25], etc. It was found generally that the substitution of Mn with other metals in (La, Sr)MnO_3 drastically lower the Curie temperature T_C and eventually lead to insulating state and/or cluster-glass-like state for higher substitutions. In addition, another study showed that Mn-site substitution by various M could not enhance the MR response at a low magnetic field of 2 KOe for $La_{0.7}Sr_{0.3}Mn_{0.9}M_{0.1}O_3$ compounds with M = Al, Cr, Fe, Co, Ni, Cu and Ga [26].

In the present work, experimental data are shown for the influence of V concentration ($0 \leq x \leq 0.15$) on phase composition, magnetic and electrical properties of La-based manganites with substitution of Mn site by the 3d magnetic element V. This compound belongs to the family of $La_{0.67}Sr_{0.33}Mn_{1-x}V_xO_3$ perovskites shown that the spontaneous magnetization and the Curie temperature T_C continuously decrease as V content increases, reaching value of T_C nearing room temperature for $La_{0.67}Sr_{0.33}MnO_3$, which is beneficial for technological applications.

2 Experimental Technique

$La_{0.67}Sr_{0.33}Mn_{1-x}V_xO_3$ ($0 \leq x \leq 0.15$) samples were prepared by the conventional ceramic fabrication technique of solid-state reaction. The starting powder reagents La_2O_3, MnO_2, $Sr(CO_3)$ and V_2O_5 were mixed in a stoichiometric proportions. Thoroughly mixed powders were ground and calcined in air at 900 °C for 72 h with intermediate grinding then pressed into pellets form under 4 t/cm^2 and finally sintered in air at 1400 C for 24 h.

The structure and phase purity of the specimens were examined by powder X-ray diffraction using Cu Kα, radiation ($\lambda_{Cu \, K\alpha} = 1.544$ Å) at room temperature in Bragg angle range $20° \leq \theta \leq 120°$ with step of 0.02° and the counting time of 18 s per step. The data were analyzed by means

of Rietveld analysis [27] (using FULL0020PROF program software). The Rietveld method uses a least squares approach to refine a theoretical line profile until it matches the measured one. The phase composition and microstructure of the sintered samples was observed by scanning electron microscopy (SEM) equipped with an energy dispersive X-ray system and the pictures were taken at room temperature on a Philips XL30 equipped with a field emission gun at 20 kV.

Magnetization (M) versus temperature (T) was recorded by using a Foner magnetometer equipped with a superconducting coil in magnetic field of 0.05 T.

In order to carry out electrical property, resistivity measurements are performed using the conventional four-probe method without applying magnetic field.

3 Results and Discussion

3.1 Scanning Electron Microscopy and Energy Dispersive Analysis

The energy dispersive X-ray analysis shows that there are no strange elements and it confirms the composition within experimental errors. The EDX spectra represented in Fig. 1 reveal the presence of all integrated elements (La, Sr, Mn, V and O), which confirms that there is no loss of anything during the sintering. In the inset of Fig. 1, the secondary electron images for samples $La_{0.67}Sr_{0.33}Mn_{1-x}V_xO_3$ with $x = 0.05$ and $x = 0.15$ were shown. These micrographs show that the samples are constituted of homogeneous particles which connect with each other. Besides, we clearly observe that the grain size is different in the two samples ($x = 0.05$, $x = 0.15$) and estimated to be mostly within (200–250 nm). This obviously indicates that the incorporation of vanadium into Mn sites promotes the grain growth during the sintering process at 1673 K. The average grain size (D) can be also calculated from the XRD peaks using the Scherrer formula:

$$D = \frac{0.9 \times \lambda}{\beta \times \cos(\theta)}$$

where λ is the X-ray wave length employed, θ is the diffraction angle for the most intense peak ($h \, k \, l \equiv (1 \, 0 \, 4)$) for all samples, and β is defined as $\beta^2 = \beta_m^2 - \beta_S^2$. Here, β_m is the experimental full width at half maximum (FWHM) and β_S is the FWHM of a standard silicon sample [28]. The as-obtained D for the samples with $x = 0$ and $x = 0.15$ are 60 nm and 86 nm significantly smaller than the values determined by SEM, which indicates that each particle observed by SEM consists of several crystallized grains.
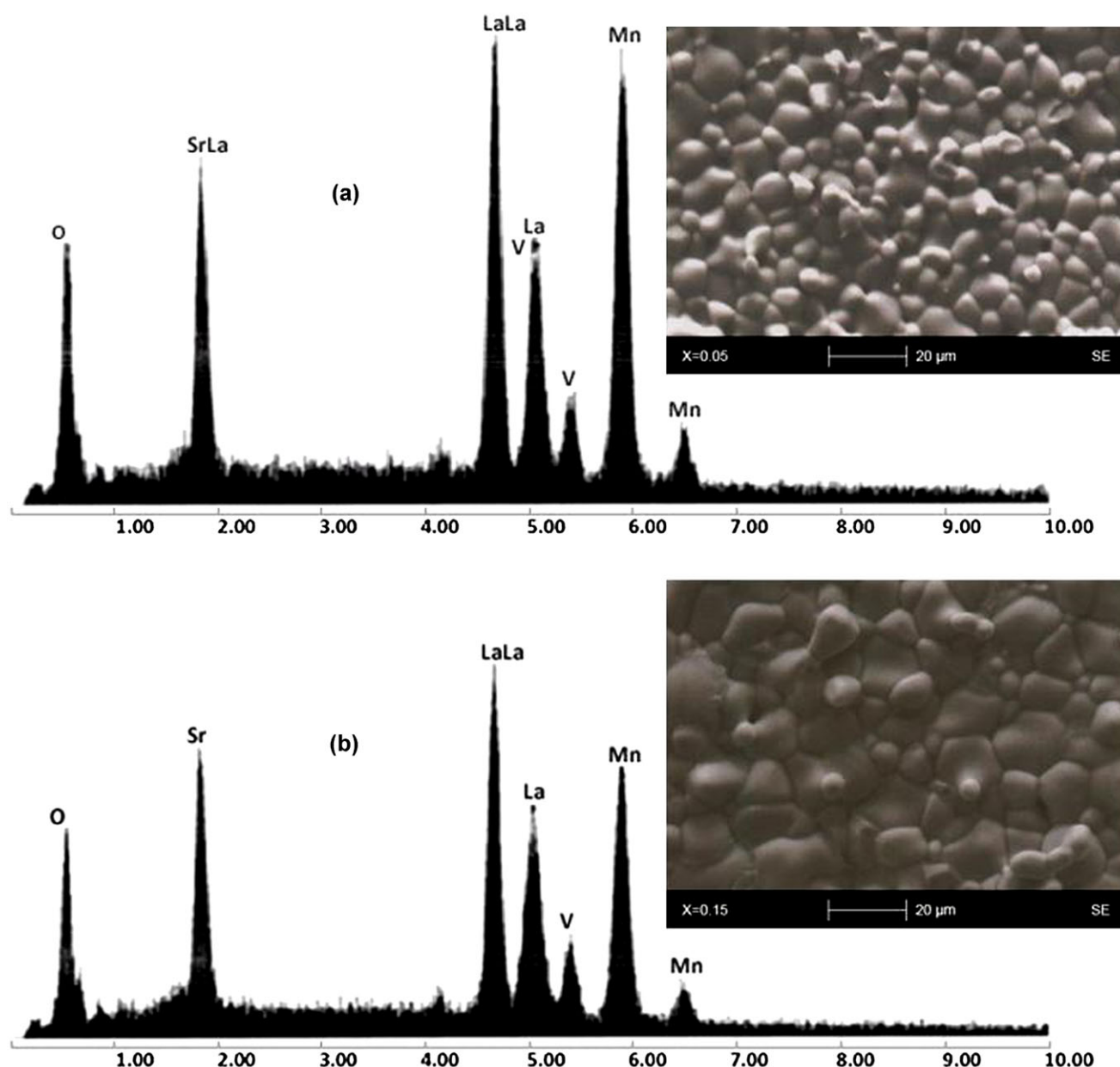
Fig. 1 Plot of EDX analysis of chemical species of $La_{0.67}Sr_{0.33}Mn_{1-x}V_xO_3$ with (**a**) $x = 0$ and (**b**) $x = 0.15$. The *inset* identifies the scanning electron micrographs (SEM)

3.2 Structural Properties

Figure 2 shows a typical example of the observed and calculated diffraction profiles of the sample with $x = 0.1$. The result of X-ray diffraction indicates that all samples are single-phase. No traces of secondary phases were detectable, within the sensitivity limits of the experiment (a few percent). The diffraction pics are indexed with respect to the rhombohedral structure with space group $R\bar{3}C$. The results of refinement are listed in Table 1, where a and c are the hexagonal cell parameters, V is the cell volume,

B_{iso} is the isotropic thermal parameter and x is the oxygen position. The residuals for the weighted patterns R_{wp}, the pattern R_p, the structure factor R_F and the goodness of fit χ^2 are also reported in this table. The final R_F of refinement was always less than 5.22, which is comparable with the results found in other work in the literature [29, 30].

We can see from Table 1 that the lattice parameters a, c and the unit-cell volume V increase monotonically with increasing V concentration. The increasing in the lattice constants and the unit-cell volume can be related to the larger ionic radius of V ion ($r_{V^{4+}} = 0.63$ Å and $r_{Mn^{4+}} =$

Fig. 2 Observed (*point symbols*) and calculated (*solid lines*) X-ray diffraction pattern for $La_{0.67}Sr_{0.33}Mn_{0.9}V_{0.1}O_3$. Positions for the Bragg reflection are marked by vertical bars. Differences between the observed and the calculated intensities are shown at the bottom of the diagram
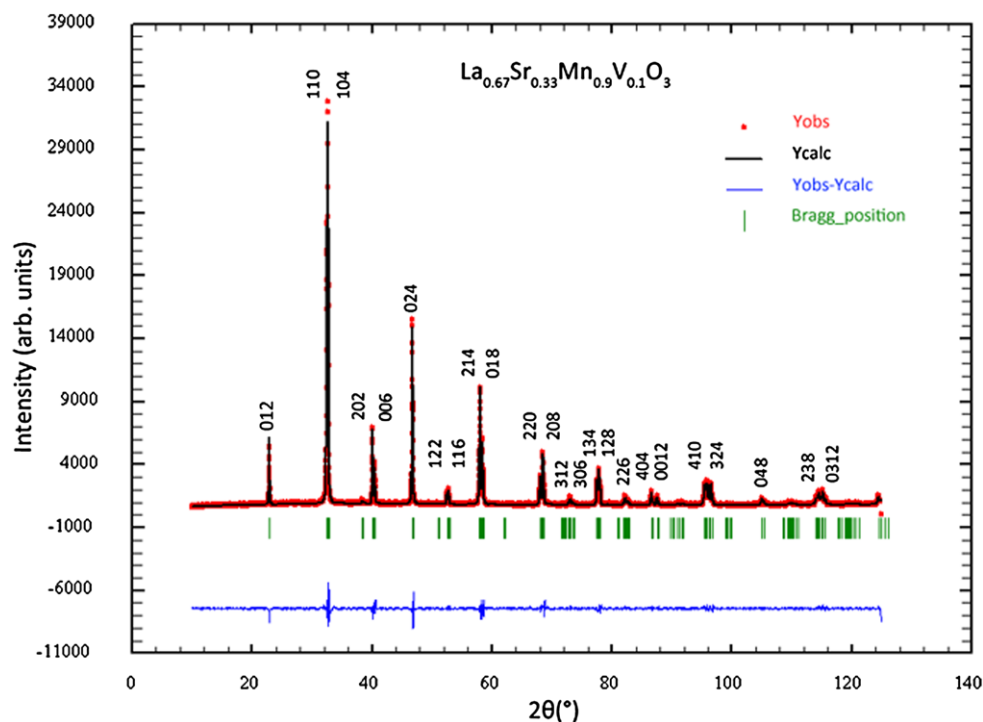

Table 1 Results of the Rietveld refinements of X-ray powder diffraction data at room temperature of $La_{0.67}Sr_{0.33}Mn_{1-x}V_xO_3$ ($0 \leq x \leq 0.15$)

|	x			
	0	0.05	0.1	0.15
$R\bar{3}c$ phase				
a (Å)	5.4933(4)	5.5044(0)	5.5093(8)	5.5164(3)
c (Å)	13.354(6)	13.360(5)	13.365(5)	13.368(2)
V (Å³)	349.11(8)	350.36(2)	351.33(1)	352.32(7)
(La/Sr)(6a) B_{iso} (Å²)	0.78(3)	1.12(6)	0.92(7)	0.90(6)
(Mn/V) (6b) B_{iso} (Å²)	0.05(3)	0.33(8)	0.18(5)	0.28(6)
(O)(18e) B_{iso} (Å²)	1.901(3)	2.611(2)	2.521(1)	2.950(1)
x(O)	0.478(2)	0.471(3)	0.467(4)	0.467(1)
Discrepancy factors				
R_{wp} (%)	5.85	7.01	6.17	6.34
R_p (%)	4.37	4.94	4.50	4.64
R_F (%)	5.22	4.25	3.15	4.06
χ^2 (%)	3.82	5.32	4.03	4.10

Space group ($R\bar{3}c$). The atomic positions are 6a (0, 0, 1/4) for La/Sr, 6b (0, 0, 0) for Mn/V; 18e (x, 0, 1/4) for oxygen

0.53 Å) [31]. This is confirmed by the Rietveld refinement of the (Mn, V)–O bond length and the (Mn, V)–O–(Mn, V) bond angles calculated from the structure parameters (see Table 2). From the results of the average distance of (Mn, V)–O and the average angles of (Mn, V)–O–(Mn, V), it is considered that each MnO_6 octahedron has little distortion. A similar result is found in $La_{0.67}Ca_{0.33}Mn_{1-x}V_xO_3$ ($0 \leq x \leq 0.1$) [32]. The rhombohedric structure distortion is indicated by the decrease of Goldsmith tolerance factor $t = r_A + r_O/\sqrt{2}(r_A + r_B)$ [33] (r_A is the average ionic radius of La^{3+} and Sr^{2+}, r_O the ionic radius of O^{2-} and r_B is the average ionic radius of Mn^{3+}, Mn^{4+} and V^{4+}) and the increase of the mean steric distortion factor D (see Fig. 3), which is defined as $D = 1/3 \sum_i |a_i - \bar{a}/a_i| \times 100$. Here $\bar{a} = (a_1 a_2 a_3)^{1/3}$, $a_1 = a_2 = a$, $a_3 = c/\sqrt{6}$, a and c are the lattice parameters [34]. Generally, the cubic struc-

Table 2 Values of average distance and angle in $La_{0.67}Sr_{0.33}Mn_{1-x}V_xO_3$ ($0 \leq x \leq 0.15$)

	x			
	0	0.05	0.1	0.15
$\theta_{(Mn,V)-O-(Mn,V)}$ (°)	174.86(3)	170.60(6)	169.34(6)	169.34(2)
$d_{(Mn,V)-O}$ (Å)	1.9413(7)	1.9472(1)	1.9491(0)	1.9518(8)
$\langle r_B \rangle$ (Å)	0.6104	0.6154	0.6204	0.6254
ω (°)	4.31	5.67	6.44	6.50
$w(10^{-2})$	9.831	9.673	9.657	9.624

Fig. 3 Compositional dependences of the tolerance factor and mean structural distortion D
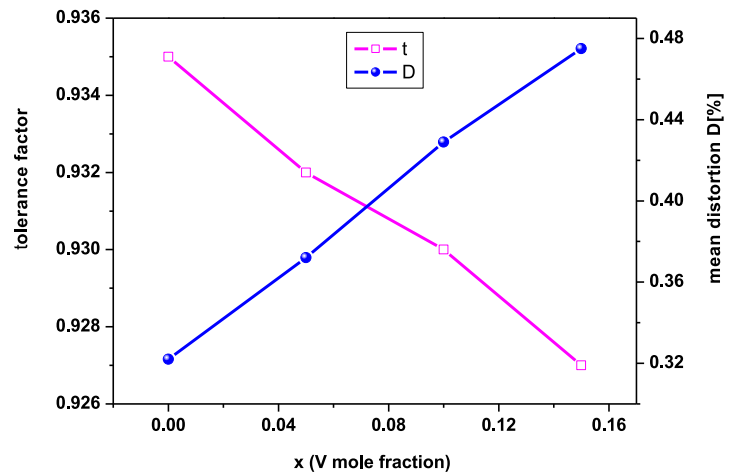
ture is distorted either by atom B moving off center in its octahedra or by the cage collapsing by rotation of the BO_6 octahedra. For the present studied system, the rhombohedral distortion may be viewed as a rotation of the octahedral around the three-fold axis by an angle ω from the ideal perovskite position. This rotation describes the buckling of the MnO_6 octahedra caused by ionic radii mismatch between A and B cations. The angle of rotation ω may be calculated from the oxygen position using $\omega = \arctan(\sqrt{3} - x\sqrt{12})$ [35]. The obtained values are listed in Table 2, indicating large distortions for all the compositions. The relation between ω and super exchange Mn–O–Mn bond angle, for regular Mn coordination octahedral, is given by $\cos\theta = (1 - \cos^2\omega)/3$ [36]. The calculated values of θ using values of ω are in reasonable agreement with that obtained from refinement (see Table 2). The departure from 180° of (Mn/V–O–Mn/V) bond angle is a measure of the distortion. The variations of the bond length $d_{(Mn/V)-O}$ and of bond angle $\theta_{(Mn/V)-O-(Mn/V)}$ have opposite effects on the unit-cell volume. For a distorted perovskite they are related by $V = z[2d_{(Mn/V)-O}\cos\omega]^3$ [37], where $\omega = [\pi - \theta_{(Mn/V)-O-(Mn/V)}]/2$ and z is the number of formula units in the unit cell ($z = 6$ in the present case). Using the observed values of $d_{(Mn/V)-O}$ and $\theta_{(Mn/V)-O-(Mn/V)}$ in the above expression, the functional dependence of volume as a function of concentration x of vanadium is reproduced.
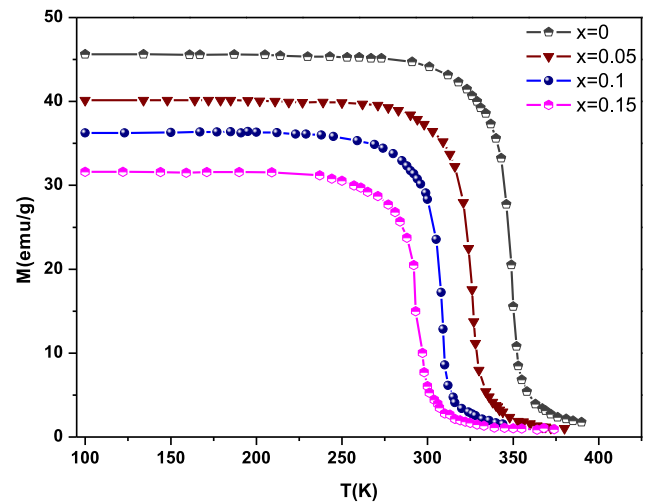
Fig. 4 Magnetization of $La_{0.67}Sr_{0.33}Mn_{1-x}V_xO_3$ ($0 \leq x \leq 0.15$) as a function of temperature measured at $H = 0.05$ T

3.3 Magnetic Characterization

Curves of temperature dependence of the magnetization obtained in a field of 0.05 T for polycrystalline $La_{0.67}Sr_{0.33}Mn_{1-x}V_xO_3$ ($0 \leq x \leq 0.15$) are shown in Fig. 4. The curves $M(T)$ do not reveal secondary magnetic phase which confirm the good crystallization of our samples. The Curie temperature T_C has been taken as the position of the minimum in the dM/dT curves (b-inset of Fig. 5) and

Fig. 5 Temperature dependence of magnetization for the sample with $x = 0.1$. The inset a is the plot of Curie–Weiss law vs. temperature, and the inset b indicates the plot of dM/dT curve for determining T_C
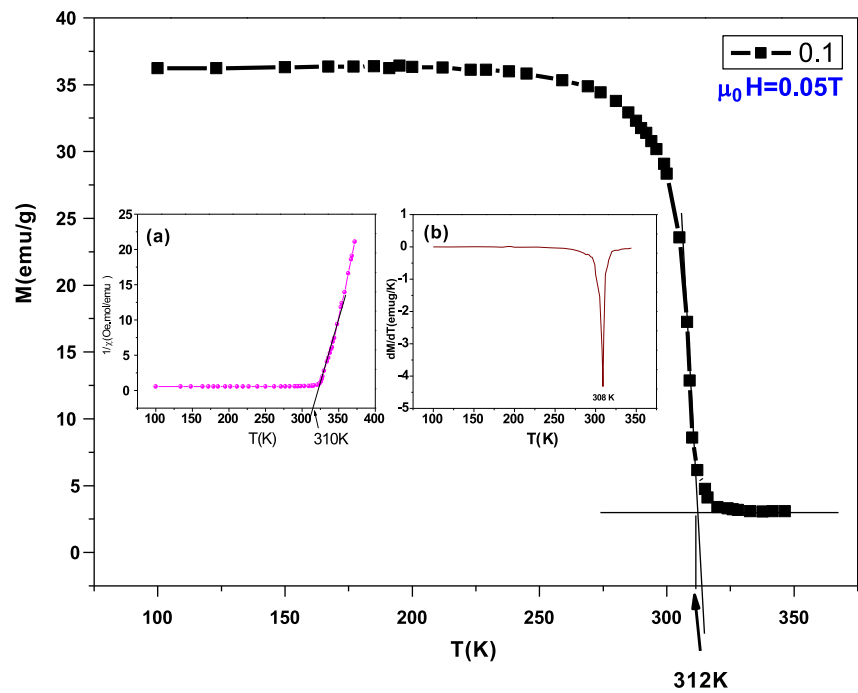

Table 3 Transition temperature T_C, T_P, Curie–Weiss temperature θ_{cw}, experimental μ_{eff}^{exp} and calculated μ_{eff}^{cal}, effective paramagnetic moments

	T_C (K)	T_p (K)	ρ_{peak} (Ω cm)	μ_{eff}^{exp} (μ_B)	μ_{eff}^{cal} (μ_B)	θ_{CW} (K)
$La_{0.67}Sr_{0.33}MnO_3$	350	329	0.063	5.19	4.58	339
$La_{0.67}Sr_{0.33}Mn_{0.95}V_{0.05}O_3$	326	309	0.090	4.88	4.50	314
$La_{0.67}Sr_{0.33}Mn_{0.9}V_{0.1}O_3$	308	289	0.104	4.70	4.44	297
$La_{0.67}Sr_{0.33}Mn_{0.85}V_{0.15}O_3$	292	280	0.116	4.37	4.37	282

has been enumerated in Table 3. We can see that the Curie temperature T_C shifts from 350 K to 292 K when the vanadium content x increases, and the spontaneous magnetization decreases with increasing vanadium content x, which is due to the decrease in the volume fraction of the ferromagnetism (FM).

We have used three methods shown in Fig. 5 in order to determine the value of Curie temperature T_C which displays the temperature dependence of magnetization of $La_{0.67}Sr_{0.33}Mn_{1-x}V_xO_3$ sample.

Method 1: A linear extrapolation of $M(T)$ to zero magnetization.

Method 2: A determination of inflection point of the transition by using the numerical derivation dM/dT as indicated in the b-inset of Fig. 5.

Method 3: A linear fit of the curve $1/\chi$ as a function of T in the paramagnetic region as shown in the a-inset of Fig. 5.

The obtained values of T_C determined by the three methods mentioned above are slightly the same.

The main factor of the decrease of T_C is that the substitution of Mn^{4+} by V^{4+} favors the super exchange interac-

tion (Mn^{4+}–O–Mn^{4+}, Mn^{3+}–O–Mn^{3+}, V^{4+}–O–V^{4+}) via oxygen 2p orbital and produces a decrease in the double-exchange interaction (Mn^{3+}–O–Mn^{4+}). In fact, since V replaces Mn site, which causes a depletion of the Mn^{3+}/Mn^{4+} ratio, the population of the hopping electrons and the number of available hopping sites decreases, so the double exchange is suppressed, resulting in the reduction of ferromagnetism as V content increases. It suggests that different transition metal introduced in Mn site gives a negative contribution to DE mechanism. Similar behavior was observed for $La_{0.57}Nd_{0.1}Pb_{0.33}Mn_{1-x}Ti_xO_3$ [38]. The T_C variation is also interpreted by the decrease of the Mn/V–O–Mn/V bond angle and the increase of the Mn/V–O bond length with V content increase as shown in Table 2. In fact, there is a direct relation between T_C and the carrier bandwidth (W) of the e_g bond, which in turn depends on the Mn–O–Mn bond angles. The empirical formula of the bandwidth W for manganites is $W \propto \cos[1/2(\pi - \theta)]/(d_{B-O})^{3.5}$, here θ is the (Mn/V–O–Mn/V) bond angle and d_{B-O} is the (Mn/V)–O bond length. Since the (Mn/V)–O–(Mn/V) bond angle is the basic structural parameter which controls the charge carrier
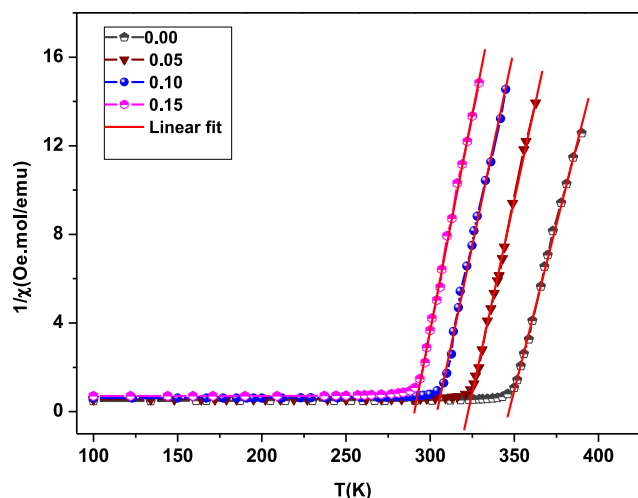
Fig. 6 The temperature dependence of the inverse of the magnetic susceptibility for $La_{0.67}Sr_{0.33}Mn_{1-x}V_xO_3$

Fig. 7 Temperature dependence of the resistivity ρ in zero field for $La_{0.67}Sr_{0.33}Mn_{1-x}V_xO_3$ ($0 \leq x \leq 0.1$). The inset is for ($x = 0.0$)

mobility, the decrement in the (Mn/V)–O–(Mn/V) bond angle with doping will change the charge carrier concentration in the system, and thus hamper the increment in T_C. At the same time, the increase of (Mn/V)–O bond length reduces the overlap between the Mn 3d and O 2p orbitals and contributes to the decrease of W, which results in the decrease in T_C.

In Fig. 6, we plotted the inverse magnetic susceptibility $\chi^{-1}(T)$ (defined as $(H/M)^{-1}$) as a function of temperature for the samples at 0.05 T. In the paramagnetic region ($T \geq T_C$), the susceptibility follows the Curie–Weiss law, i.e. $\chi = C/(T - \theta_{CW})$, where θ_{CW} the Curie-Weiss temperature and C is the Curie constant. The temperature at which $1/\chi$ intercepts the temperature axis is the Curie-Weiss temperature θ_{CW} and the Curie constant C were obtained by fitting the linear paramagnetic region of the data (Fig. 6); then the experimental effective paramagnetic moments, μ_{eff}^{exp}, were calculated using the C values in the equation $C = (\mu_0/3K_B)\mu_{eff}^2$. The effective paramagnetic moments can be also obtained theoretically using this formula: $\mu_{eff}^{cal} = \sqrt{0.67[\mu_{eff}^{th}(Mn^{3+})]^2 + (0.33 - x)[\mu_{eff}^{th}(Mn^{4+})]^2 + x[\mu_{eff}^{th}(V^{4+})]^2}$, with $\mu_{eff}^{th}(Mn^{3+}) = 4.9\mu_B$, $\mu_{eff}^{th}(Mn^{4+}) = 3.87\mu_B$ and $\mu_{eff}^{th}(V^{4+}) = 1.55\mu_B$ [39]. The Curie-Weiss temperature θ_{CW}, μ_{eff}^{exp} and μ_{eff}^{cal} are summarized in Table 3. We see in this table that the experimental values of the effective paramagnetic moments μ_{eff}^{exp} are close to the calculated one μ_{eff}^{cal}. The positive values of θ_{CW} indicate the ferromagnetic interaction between spins.

3.4 Electrical Properties

The results of resistivity $\rho(T)$ obtained under zero applied field are shown in Fig. 7 for $La_{0.67}Sr_{0.33}Mn_{1-x}V_xO_3$ with $x = 0$, 0.05, 0.1 and 0.15. For e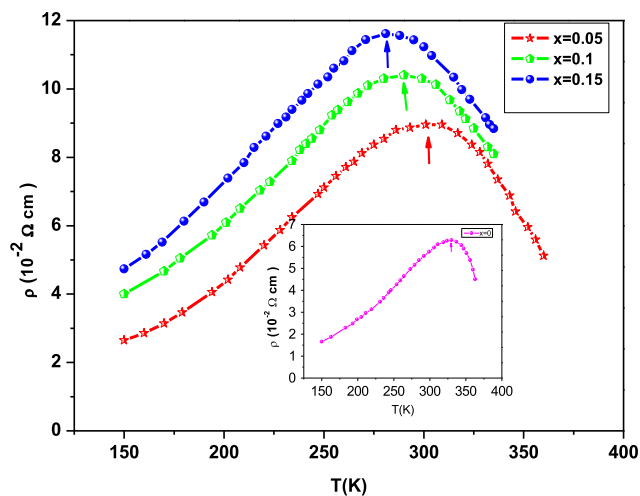ach of the samples the resistivity ρ_{max} increases monotonically with increasing the content of V. Using the sign of the temperature coefficient of the resistivity $d\rho/dT$ as a criterion, we found that for $0 \leq x \leq 0.15$, these compounds are ferromagnetic-metallic at low temperature ($T < T_p$) and become paramagnetic–semiconductor above the temperature peak T_P. The metal-semiconductor transition T_P, which is indicated by arrows in Fig. 7, decreases to a lower temperature (see Table 3). Similar behavior was observed for Co-substituted manganites $La_{0.67}Pb_{0.33}Mn_{1-x}Co_xO_3$ [40]. The observed behavior may originate from several contributions. First of all, the higher radius of V leads to a decrease in the (Mn/V)–O–(Mn/V) angle and an increase of the average (Mn, V)–O distance, which reduces the ferromagnetic coupling between neighbor manganese and decrease the degree of metal-oxygen overlap and the bandwidth. This phenomenon can also be explained in terms of the double-exchange model, in which electrons in the e_g level of Mn^{3+} ions become itinerant between Mn^{3+} and Mn^{4+} in this system. When Mn ions are partially substituted with other elements (V) having different electronic structures, the electron conduction paths are broken. The reduction of T_P and higher resistivity is a natural consequence. Besides, the substitution of Mn^{4+} by V^{4+} reduces the number of Mn^{3+}–O–Mn^{4+} network, responsible of conduction in perovskite materials.

Figure 8 shows the dependence of the magnetic transition temperatures (T_C) and the metal-semiconductor transition (T_P) vs. x. The two transition temperatures T_C and T_P decrease but worth mentioning that the T_P of all samples is lower than their respective T_C. This difference may be ascribed to the microstructural effect like oxygen variation or grain boundaries which dominate the transport properties.

Fig. 8 Variation of the magnetic transition temperatures (T_C) and the metal-semiconductor transition (T_P) with x for $La_{0.67}Sr_{0.33}Mn_{1-x}V_xO_3$
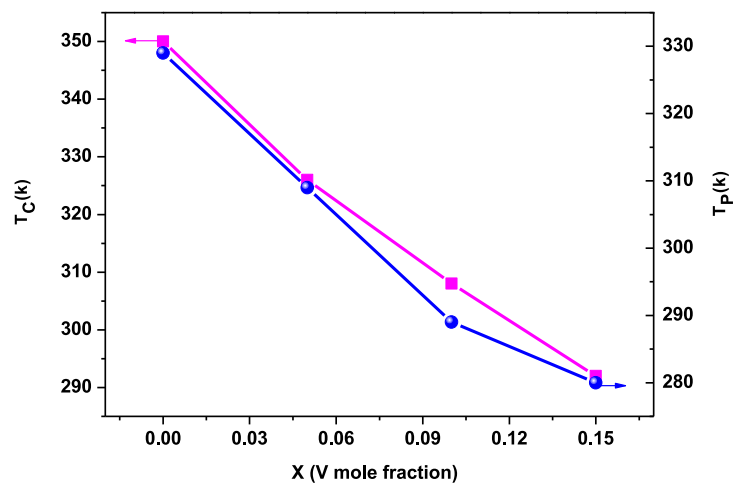
3.5 Conduction Mechanism

3.5.1 Low Temperature Behavior ($T < T_P$)

To explain the low temperature regime where the transport properties fully show the metallic state (below T_P), the temperature dependence of the resistivity can be generally fitted using three different expressions for resistivity: $\rho = \rho_0 + \rho_2 T^2$. ρ_0 represents the resistivity due to the grain/domain boundary effects [41] and the $\rho_2 T^2$ term indicates the contribution from the electron–electron scattering process [42, 43]. The ansatz $\rho = \rho_0 + \rho_{2.5} T^{2.5}$ can be also used to fit the low temperature resistivity regime. This equation was previously used by Venkataiah et al. [44]. Here, the $\rho_{2.5} T^{2.5}$ term represents single-magnon scattering in the ferromagnetic phase [45, 46]. $\rho = \rho_0 + \rho_2 T^2 + \rho_{4.5} T^{4.5}$ is the third expression which can be utilized to explain the conduction mechanism in a double-exchange system in the ferromagnetic region. The term $\rho_{4.5} T^{4.5}$ is a combination of the electron–electron, the electron–magnon and the electron–phonon scattering processes [47]. In order to find which model is best suited for the present system as well as the nature of interaction, we have first tried to fit the metallic part of the resistivity curve with all these three empirical equations containing. After comparing the square of a linear correlation coefficient (R^2) obtained for each equation, we have found that in the metallic regime, the resistivity can be fitted well with equations of the form $\rho = \rho_0 + \rho_2 T^2 + \rho_{4.5} T^{4.5}$. The values of R^2 of this equation were as high as 99.9 %, which ensures that the transport mechanism in this regime can be attributed to the electron–magnon scattering. The fitted data are shown by red solid lines in the main panel of Fig. 9. The best fit parameters obtained are shown in Table 4. These values are comparable to those reported in mixed valent manganites [36]. Table 4 shows that ρ_0 remarkably increases with increasing V-doping level, implying that the V-doping results in the enhancement of the domain or grain

boundary scattering. In addition, the obvious increase of ρ_2 can be attributed to the suppression of spin fluctuation. Therefore, the bandwidth becomes smaller. Consequently, it can be concluded that the strength of the electron–magnon scattering term depends not only on the grain growth, but also on how the grain growth has been achieved.

3.5.2 High Temperature Behavior ($T > T_P$)

The high temperature electronic transport properties can be explained by two different models, the variable range hopping (VRH) and the adiabatic small polaron hopping (SPH) model [48], which is considered at temperatures beyond $\theta_D/2$, θ_D is the Debye temperature, which is determined from the plots of $\ln(\rho/T)$ vs. $1/T$ (b-inset of Fig. 9). This latter model is used in the region ($T > \theta_D/2$), where the conduction mechanism is governed by thermally activated small polarons. In this case, the resistivity is expressed by $\rho = \rho_0 \exp(E_a/K_B T)$ [49]. Here ρ_0 is a pre-exponential coefficient, E_a is the activation energy and K_B is the Boltzmann constant. The activation energies (E_a) values calculated in the best-fit parameters are described in Table 4 and the corresponding plot is shown in b-inset of Fig. 9 for $x = 0.05$. It is clear from Table 4 that the activation energy (E_a) values are increasing with the increase of V content. The observed behavior reflects the increase in polaron more clearly than Mn ions in the lattice.

In order to explain the electrical conduction slightly above T_P, i.e. $T_P < T < \theta_D/2$, we used the VRH model, which employs the Mott law equation $\sigma = \sigma_0 \exp(-T_0/T)^{1/4}$, where T_0 is the characteristic temperature, $T_0 = 16\alpha^3/K_B N(E_F)$, here $N(E_F)$ is the density of states at the Fermi level. The value of α (the localization length of electrons in the paramagnetic state) is considered as 2.22 nm^{-1} as is calculated by Viret et al. [50]. The estimated values of T_0 and $N(E_F)$ are given in Table 4. It is noticed that the values of $N(E_F)$ are decreasing with

Fig. 9 The main panel represents the plots of the electrical resistivity $\rho(T)$ vs. T for $La_{0.67}Sr_{0.33}Mn_{0.95}V_{0.05}O_3$. The *bold solid line* in these plots represents the best fit of experimental data in the metallic regime, below T_P with the equation $\rho = \rho_0 + \rho_2 T^2 + \rho_{4.5} T^{4.5}$. The (**a**) *inset* correspond to the fit of data in the semiconductor region $(T_P < T < \theta_D/2)$, with equation $\sigma = \sigma_0 \exp(-T_0/T)^{1/4}$. The (**b**) *inset* corresponds to the fit of data above $\theta_D/2$, with the equation $\rho = \rho_0 \exp(E_a/K_B T)$
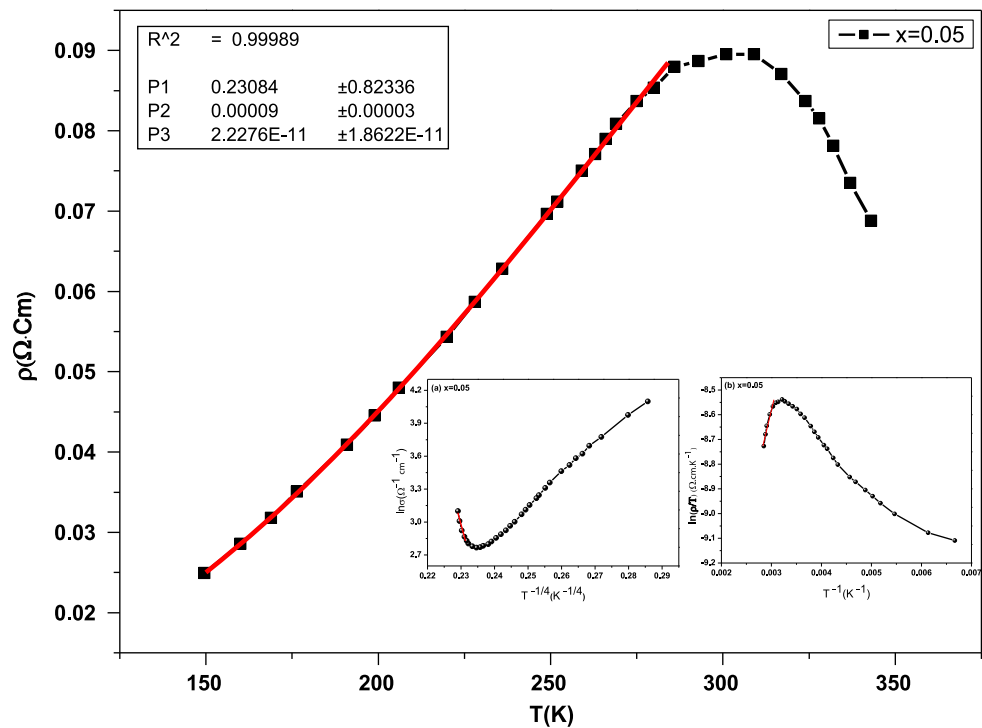

Table 4 The best fit parameters obtained from the experimental resistivity data for the metallic behavior (below T_P) and for semiconductor behavior (above T_P) for $La_{0.67}Sr_{0.33}Mn_{1-x}V_xO_3$ ($x = 0.0$–0.15) compounds

Sample code	$\rho = \rho_0 + \rho_2 T^2 + \rho_{4.5} T^{4.5}$			$\sigma = \sigma_0 \exp(-T_0/T)^{1/4}$				$\rho = \rho_0 \exp(E_a/k_B T)$	
	$\rho_0 (\Omega\,cm)$	$\rho_2 (\Omega\,cm\,K^{-2})$	$\rho_{4.5} (\Omega\,cm\,K^{-4.5})$	R^2	$T_0 (\times 10^7\,K)$	$N(E_F)$	$\theta_D(k)$	$\upsilon_{ph} (\times 10^{12}\,Hz)$	E_a (meV)
$x = 0.00$	0.217	6×10^{-5}	3.423×10^{-12}	0.9992	0.22	9.23×10^{-22}	749	15.61	59.70
$x = 0.05$	0.230	9×10^{-5}	2.227×10^{-11}	0.9998	0.41	4.92×10^{-22}	729	15.19	63.88
$x = 0.10$	0.100	11×10^{-5}	1.827×10^{-11}	0.9996	4.05	5.01×10^{-23}	684	14.25	128.19
$x = 0.15$	1.931	12×10^{-5}	1.438×10^{-11}	0.9970	6.56	3.09×10^{-23}	628	13.09	131.53

the increase of the concentration of vanadium due to the decrease in the DE interaction. The optical phonon frequencies or attempt frequency (υ_{ph}) can also be obtained from the relation ($h\upsilon_{ph} = K_B\theta_D$), h is Planck's constant ($h = 6.62 \times 10^{-34}$ J.s). It is clear from Table 4 that the values of phonon frequency and $\theta_D/2$ decreased against vanadium concentration and it seems that the values $\theta_D/2$ are much higher than T_P, which highlights the width of VRH region between $\theta_D/2$ and T_P.

4 Conclusions

In summary, we have investigated the structural, magnetic and transport properties of polycrystalline samples with nominal composition of $La_{0.67}Sr_{0.33}Mn_{1-x}V_xO_3$ ($0 \le x \le 0.15$) which have been synthesized by using the standard ceramic process. Using the Rietveld refinement of X-ray pow-

der diffraction, it is found that these compounds crystallize in the rhombohedral structure with $R\bar{3}C$ space group. Both lattice parameters and unit-cell volume V increase monotonically with increasing V concentration due to the replacement of smaller Mn^{4+} ions by larger V^{4+} ions. The magnetic measurement shows a single paramagnetic to ferromagnetic transition and the Curie temperature decreases with increasing V-doping which can be explained by the feebleness of the double-exchange interaction. The electrical studies indicate that our compounds show a metal to semiconductor transition with a decrease in the T_P with increasing V content. It is also found that in the metallic regime and at low temperature ($T < T_P$), the electrical conduction mechanism can be clarified by the grain boundary effects and the single electron-magnon scattering process. While, in the high temperature ($T > T_P$), the variable range hopping mechanism (VRH) and adiabatic small polaron hopping (SPH) mechanism can be used.

References

1. Salamon, M.B., Jaime, M.: Rev. Mod. Phys. **73**, 583 (2001)
2. Zhou, X.F., Zhao, Y., Cao, X., Xue, Y.F., Xu, D.P., Jiang, L., Su, W.H.: Mater. Lett. **62**, 47 (2008)
3. Millar, L., Taherparvar, H., Filkin, N., Slater, P., Yeomans, J.: Solid State Ion. **179**, 73 (2008)
4. Siwatch, P.K., Siugh, H.K., Srivastava, O.N.: J. Phys. Condens. Matter **20**, 273201 (2008)
5. Rodriguez-Martinez, L.M., Attfield, J.P.: Phys. Rev. B **54**, 15622 (1996)
6. Vanitha, P.V., Santosh, P.N.S., Singh, R.S., Rao, C.N.R., Attfield, J.P.: Phys. Rev. B **59**, 13539 (1999)
7. Zener, C.: Phys. Rev. **82**, 403 (1951)
8. Dhahri, A., Dhahri, J., Zemni, S., Oumezzine, M., Said, M., Vincent, H.: J. Alloys Compd. **450**, 12–17 (2008)
9. Dagotto, E.: New J. Phys. **7**, 67 (2005)
10. Ibrahim, N., Yahya, A.K., Rajput, S.S., Keshri, S., Talari, M.K.: J. Magn. Magn. Mater. **323**, 2179–2185 (2011)
11. Ata-Allah, S.S., Mostafa, M.F., Heiba, Z., Refai, H.S.: Physica B **406**, 801–811 (2011)
12. Varshney, H.D., Choudhary, D., Shaikh, M.W., Khan, E.: Eur. Phys. J. B **76**, 327–338 (2010)
13. Kalyana Lakshmi, Y., Venugopal Reddy, P.: J. Alloys Compd. **470**, 67 (2009)
14. Bhargava, S.C., Singh, S., Malik, S.K.: J. Magn. Magn. Mater. **311**, 594–604 (2007)
15. Battabyal, M., Dey, T.K.: Physica B **367**, 40–47 (2005)
16. Hwang, H.Y., Cheong, S.-W., Ong, N.P., Batlogg, B.: Phys. Rev. Lett. **77**, 2041 (1996)
17. Raychaudhuri, P., Sheshadri, K., Taneja, P., Bandyopadhyay, S., Ayyub, P., Nigam, A.K., Pinto, R., Chaudhary, S., Roy, S.B.: Phys. Rev. B **59**, 13919 (1999)
18. Tkachuk, A., Rogacki, K., Brown, D.E., Dabrowski, B., Fedro, A.J., Kimall, C.W., Pyles, B., Xiong, X., Rosenmann, D., Dunlap, B.D.: Phys. Rev. B **57**, 8509 (1998)
19. Zhang, J.H., Fan, X.J., Xiong, C.S., Li, X.-G.: Solid State Commun. **115**, 531 (2000)
20. Chen, X., Wang, Z.H., Cai, J.W., Shen, B.G., Zhanand, W.S., Chen, J.S.: J. Appl. Phys. **86**, 4534 (1999)
21. Feng, J.-W., Ye, C., Huang, L.-P.: Phys. Rev. B **61**, 12271 (2000)
22. Kallel, N., Dezanneau, G., Dhahri, J., Oumezzine, M., Vincent, H.: J. Magn. Magn. Mater. **261**, 56 (2003)
23. Qin, H.W., Hu, J.F., Chen, J., Niu, H.D., Zhu, L.M.: J. Magn. Magn. Mater. **263**, 249 (2003)
24. Sawaki, Y., Takenaka, K., Osuka, A., Shiozaki, R., Sugai, S.: Phys. Rev. B **61**, 11588 (2000)
25. Belous, A.G., V'yunov, O.I., Yanchevskii, O.Z., Tovstolytkin, A.I., Golub, V.O.: Inorg. Mater. **42**, 286 (2006)
26. Zhao, T.-S., Xianyu, W.X., Li, B.H., Qian, Z.N.: J. Alloys Compd. (2007). doi:10.1016/j.jalcom.2007.04.302
27. Rietveld, H.M.: J. Appl. Crystallogr. **2**, 65 (1969)
28. Guinier, A.: Théorie et Technique de la Radiocristallographie, 3rd edn., p. 462. Dunod, Paris (1964)
29. Gasmi, A., Boudard, M., Zemni, S., Hippert, F., Oumezzine, M.: J. Phys. D, Appl. Phys. **42**, 225408 (2009)
30. Dhahri, J., Dhahri, A., Oumezzine, M., Dhahri, E.: J. Magn. Magn. Mater. **320**, 2613–2617 (2008)
31. Shannon, R.D.: Acta Crystallogr. A, Found. Crystallogr. **32**, 751–764 (1976)
32. Nisha, P., Savitha Pillai, S., Darbandi, A., Misra, A., Suresh, K.G., Varma, M.R., Hahn, H.: J. Phys. D, Appl. Phys. **43**, 135001 (2010)
33. Jonker, G.H., Van Santen, J.H.: Physica **16**, 337–349 (1950)
34. Moritomo, Y., Asamitsu, A., Tokura, Y.: Phys. Rev. B **51**, 16491–16494 (1995)
35. Rodriguez, E., Alvarez, I., Lopez, M.L., Veiga, M.L., Pico, C.: J. Solid State Chem. **148**, 479–486 (1999)
36. Keeffe, M.O., Hyde, B.G.: Acta Crystallogr., B Struct. Crystallogr. Cryst. Chem. **33**, 3802 (1977)
37. Radaelli, P.G., Iannone, G., Marezio, M., Hwang, H.Y., Cheong, S.-W., Jorgensen, J.D., Argyriou, D.N.: Phys. Rev. B **56**, 8265 (1997)
38. Dhahri, A., Dhahri, J., Hlil, E.K., Dhahri, E.: J. Supercond. Nov. Magn. (2012). doi:10.1007/s10948-012-1485-5
39. Kittel, C.: Introduction to Solid State Physics, 6th edn., pp. 404–406. Wiley, New York (1986)
40. Dhahri, N., Dhahri, A., Cherif, K., Dhahri, J., Taibi, K., Dhahri, E.: J. Alloys Compd. **496**, 69–74 (2010)
41. Snyder, G.J., Hiskes, R., DiCarolis, S., Beasley, M.R., Geballe, T.H.: Phys. Rev. B **53**, 14434–14444 (1996)
42. Banerjee, A., Pal, S., Chaudhuri, B.K.: J. Chem. Phys. **115**, 1550–1559 (2001)
43. Urushibara, A., Morimoto, Y., Arima, T.: Phys. Rev. B **51**, 14103–14109 (1995)
44. Venkataiah, G., Krishna, D.C., Vithal, M., Rao, S.S., Bhat, S.V., Prasad, V., Subramanyam, S.V., Venugopal Reddy, P.: Physica B **357**, 370 (2005)
45. De Teresa, J.M., Ibarra, M.R., Blasco, J., Garcia, J., Marquina, C., Algarabel, P.A., Arnold, Z., Kamenev, K., Ritter, C., Von Helmolt, R.: Phys. Rev. B **54**, 1187–1193 (1996)
46. Pi, L., Zheng, L., Zhang, Y.: Phys. Rev. B **61**, 8917–8921 (2000)
47. Ewe, L.S., Hamadneh, I., Salama, H., Hamid, N.A., Halim, S.A., Abd-Shukor, R.: Appl Phys A, 457–463 (2009)
48. Mott, N.F., Davis, E.A.: Electronic Process in Non-crystalline Materials. Clarendon, Oxford (1971)
49. Snyder, G., Hiskes, R., DiCarolis, S., Beasley, M., Geballe, T.: Phys. Rev. B **53**, 1 (1996)
50. Viret, M., Ranno, L., Coey, J.M.D.: Phys. Rev. B **55**, 8067–8070 (1997)